

Submitted to ApJ

***Chandra* Observation of the Trifid Nebula: X-ray emission from the O star complex and actively forming Pre-main sequence stars**

Jeonghee Rho and Solange V. Ramírez

*SIRTF Science Center, Mail Stop 220-06, California Institute of Technology.*Michael F. Corcoran¹ and Kenji Hamaguchi*Code 662, NASA/Goddard Space Flight Center, Greenbelt, MD 20771*

Bertrand Lefloch

Laboratoire d'Astrophysique, Observatoire de Grenoble, BP 53, F-38041, Grenoble CEDEX9, France

ABSTRACT

The Trifid Nebula, a young star-forming HII region, was observed for 16 hours by the ACIS-I detector on board of the *Chandra* X-ray Observatory. We detected 304 X-ray sources, thirty percent of which are hard sources and seventy percent of which have near-infrared counterparts. *Chandra* resolved the HD164492 multiple system into a number of discrete X-ray sources. X-ray emission is detected from components HD164492A (an O7.5III star which ionizes the nebula), B and C (a B6V star), and possibly D (a Be star). Component C is blended with an unidentified source to the NW. HD164492A has a soft spectrum ($kT \approx 0.5$ keV) while the component C blend shows much harder emission ($kT \approx 6$ keV). This blend and other hard sources are responsible for the hard emission and Fe K line seen by *ASCA*, which was previously attributed entirely to HD 164492A. The soft spectrum of the O star is similar to emission seen from other single O stars and is probably produced by shocks within its massive stellar wind. Lack of hard emission suggests that neither a magnetically confined wind shock nor colliding wind emission is important in HD164492A. A dozen stars are found to have flares in the field and most of them are pre-main sequence stars (PMS). Six sources with flares have both optical and 2MASS counterparts. These counterparts are not embedded and thus it is likely that these sources are in a later stage of PMS evolution, possibly Class II or III. Two flare sources did not have any near-IR, optical, or radio counterparts. We suggest these X-ray flare stars are in an early pre-main sequence

¹Universities Space Research Association, 7501 Forbes Blvd, Ste 206, Seabrook, MD 20706

stage (Class I or earlier). We also detected X-ray sources apparently associated with two massive star forming cores, TC1 and TC4. The spectra of these sources show high extinction and X-ray luminosities of $2 - 5 \times 10^{31}$ erg s⁻¹. If these sources are Class 0 objects, it is unclear if their X-ray emission is due to solar-type magnetic activities as in Class I objects, or some other mechanism.

Subject headings: stars: activity — stars: pre-main sequence — X-rays: stars

1. Introduction

Despite of the fact that X-ray observations of star-forming regions have been a powerful tool for discovering young stellar objects (YSO) and T Tauri stars (TTS) since *Einstein* (references in Feigelson & Montmerle 1999), long wavelength (IR and submillimeter) emission is used to define evolutionary classes for young stars. Classes I-III are solely based on the excess seen in the IR spectral energy distribution (SED) with respect to stellar blackbody photospheric emission, as measured by the spectral index $\alpha_{IR} = d \log (\lambda F_\lambda) / d \log \lambda$ between $\lambda = 2.2$ and $10\text{-}25\mu\text{m}$: Class I, II and III correspond to $\alpha_{IR} > 0$, $-2 < \alpha_{IR} < 0$, and $\alpha_{IR} < -2$ (Lada 1987). Class 0 stars represent the earliest phase of star formation and are identified by the ratio of submillimeter to bolometric luminosity (André et al. 1993) and are seen as condensations in submillimeter far-infrared dust continuum maps; these condensations often show collimated CO outflows or internal heating sources. X-ray bright T Tauri stars usually belong to either Class II or III.

High resolution images obtained by the *Chandra* X-ray Observatory open a new era in the study of star formation because the 1'' resolution of *Chandra* is necessary to resolve individual sources in nearby star forming regions, and because confusion due to foreground and background stars is much less important at X-ray energies than in the optical and near-infrared regime. Recent *Chandra* observations of Orion (Garmire et al. 2000; Feigelson et al. 2002) detected hundreds of X-ray sources, e.g. pre-main sequence stars (PMS) with masses in the range $0.05 M_\odot - 50 M_\odot$ and a combined infrared and X-ray study suggests that the X-ray luminosity of PMS depends on stellar mass, rotational history, and magnetic field (Garmire et al. 2000). A high percentage of Class I PMS were also found to be X-ray emitters; in ρ Oph, 70% of identified Class I stars are X-ray bright. Strong X-ray flares from PMS in ρ Oph (Imanishi et al. 2001), Monoceros R2 (Kohn et al. 2002), and Orion (Feigelson et al. 2002) were detected from Class I, II and III objects, possibly because of magnetic activity. Moreover, X-ray emission from Class 0 candidates was detected in OMC-3 (Tsuboi et al. 2001).

The Trifid Nebula (M20) is one of the best-known astrophysical objects. It is a classical nebula ionized by an O7.5 star, HD164492A, and the ionized nebula glows in red light. The nebula is trisected by obscuring dust lanes giving the Trifid its name. A blue reflection nebula appears to the north of the red nebula. At an age of $\sim 3 \times 10^5$ years, the Trifid is a young H II region. Recent studies using the Infrared Space Observatory (ISO) and the Hubble Space Telescope (HST)

(Cernicharo et al. 1998; Lefloch & Cernicharo 2000; Hester et al. 1999) show the Trifid to be a dynamic, “pre-Orion” star forming region containing young stars undergoing episodes of violent mass ejection, with protostars like HH399 (Lefloch et al. 2002) losing mass and energy to the nebula in optically bright jets. Four massive ($17\text{--}60\text{ M}_{\odot}$) protostellar cores were discovered in the Trifid from millimeter-wave observations. These cores are associated with molecular gas condensations at the edges of clouds (Lefloch & Cernicharo 2000). T Tauri stars and young stellar object candidates were also identified using near-infrared color-color diagrams from 2MASS data (Rho et al. 2001). Unlike better-studied nearby star-forming regions such as Orion and ρ Oph, star forming activities in the Trifid have only recently been recognized (Cernicharo et al. 1998), and as a result of this (and also due to contamination by foreground and background stars in the optical and IR), the population of PMS in the Trifid has not been fully investigated. The distance to the Trifid Nebula is between 1.68 and 2.84 kpc (Lynds et al. 1985; Kohoutek et al. 1999 and references therein) and a distance of 1.68 kpc is adopted in this paper.

In this paper, we report results of *Chandra* observations of the Trifid Nebula. *Chandra* resolved the HD 164492 multiple system into a number of discrete X-ray sources and we present their X-ray properties which include components A (an O star), C (a B6V star) and B (A2Ia). Our *Chandra* observations revealed 304 sources and we found that 30% of the sources have hard emission similar to that from PMS. Among these candidate PMS, we report properties of about a dozen flare sources, which include unusual variability from the O star and unusual emission from an A-type supergiant. We also discuss the X-ray properties of the HD 164492 complex, the properties of X-ray sources which are apparently associated with two protostellar cores, and also the properties of some apparently strongly variable objects.

2. Observations

The Trifid Nebula was observed with the Advanced CCD Imaging Spectrometer (ACIS) detector on board the *Chandra X-ray Observatory* (Weisskopf et al. 2002) on 2002 June 13. The results presented here arise from the imaging array (ACIS-I), which consists of four 1024×1024 front-side illuminated CCDs. The array was centered at R.A. $18^{\text{h}}02^{\text{m}}28^{\text{s}}$ and Dec. $-22^{\circ}56'50''$ (J2000) and covered an area in the sky of about $17' \times 17'$. The total exposure time of the ACIS observations was 58 ksec. This observation is sensitive to X-ray luminosities of $5 \times 10^{29}\text{ erg s}^{-1}$, assuming an appropriate PMS X-ray spectrum (temperature of 1 keV and an absorption $1.6 \times 10^{21}\text{ cm}^{-1}$) at the distance (1.68 kpc) of the Trifid.

We started data analysis with the Level 1 processed event list provided by the pipeline processing at the *Chandra X-ray Center*. The energy and grade of each data event were corrected for charge transfer inefficiency (CTI), applying the algorithm described by Townsley et al. (2000). The event file was filtered to include event grades of 0, 2, 3, 4, and 6, and filtered by time intervals to exclude background flaring intervals or other bad times. The filtering process was done using

the *Chandra* Interactive Analysis of Observations (CIAO) package¹ provided by the *Chandra* X-ray Center.

Figure 1 shows the *Chandra* ACIS-I three color image of the Trifid. Hundreds of point sources are detected with little diffuse emission. X-ray sources were located using the *wavdetect* tool within the CIAO package. This tool performs a Mexican hat wavelet decomposition and reconstruction of the image after accounting for the spatially varying point spread function as described by Freeman et al. (2002). We used wavelet scales ranging from 1 to 16 pixels in steps of $\sqrt{2}$, and a default source threshold probability of 1×10^{-6} . The *wavdetect* tool was run using an exposure map and it produced a catalog of 353 sources from the entire ACIS-I FOV. Then we identified false sources produced by cosmic rays or cases in which the source counts are below the background counts. This observation finally resulted in 304 X-ray sources detected from the total ACIS-I FOV ($17' \times 17'$). The full source list is given in Table 1 in order of R.A. Thirty percent of these sources are shown to be hard (shown in blue in Figure 1); the hard sources have a spectral hardness ratio (SHR) > -0.2 , where SHR is the ratio of the net counts in the hard 2.0 – 8.0 keV band to those in the soft 0.5 – 2.0 keV band. Diffuse emission was not obvious in the *Chandra* images of the Trifid Nebula with our current data processing. None-detection of diffuse emission in M20 is consistent with a claim that high mass star-forming regions without stars earlier than O6 may be unlikely to exhibit diffuse soft X-rays (Townsend et al. 2003; Abbott 1982)

The brightest source in the field corresponds to the O star HD164492A (source 102) and has 884 counts. This is equivalent to 0.047 photons per frame, which is small enough so as not to be affected by pileup effects (the pileup fraction is < 0.05). In order to verify the hard emission and Fe K line detected in the *ASCA* spectra of HD164492A (Rho et al. 2001), we extracted a spectrum using the same extraction region as was used in the *ASCA* analysis, and confirmed that the *Chandra* and *ASCA* spectra are the same within the errors. However, we found that HD164492A is actually a soft source (see section 6 for details) while the hard emission and Fe K line (which were attributed to the O star in the *ASCA* analysis) is actually produced by the hard sources resolved by *Chandra* as shown Figure 2. In addition, the emission previously attributed entirely to HD164492A in an analysis of *ROSAT* PSPC data (Rho et al. 2001) is now resolved into a dozen X-ray sources as shown in Figure 1 and 2.

To confirm the X-ray astrometry, we used the 2MASS² final release point source catalog to search for near-IR counterparts to the X-ray sources in the full source list. We cross-correlated the positions of the 2MASS sources with the positions of our X-ray sources. Within $5'$ of the *Chandra* aimpoint, we found 72 2MASS sources that coincide with X-ray source positions. We computed the total R. A. and DEC offset of these sources and obtained offsets of $-0.16''$ in R. A., and $-0.09''$ in DEC, which are less than one third of a pixel. Therefore, the astrometry of Trifid ACIS image

¹<http://cxc.harvard.edu/ciao/index.html>

²<http://www.ipac.caltech.edu/2mass>

was confirmed with the minor systematic errors in the *Chandra* aspect solution.

3. The Multiple System HD164492

The HD164492 complex is a multiple stellar system composed of 7 physically related components, A-G (Kohoutek et al. 1999). Component HD164492A is the O7.5 III((f)) star responsible for ionizing the nebula. This complex was observed as an unresolved bright X-ray source in PSPC images (Rho et al. 2001). Our *Chandra* images (Figures 1 and 2) resolve this complex into a number of discrete X-ray sources. X-ray emission is clearly detected from components A, B, and C as shown in Table 2 (Fig. 2). HD164492A is the brightest X-ray source in this complex. Component HD164492C (a B6V star, Gahm et al. 1983) is a bright X-ray source (source 94) and is barely resolved from a nearby X-ray source to the NW of C (source 91) which has no obvious optical counterpart (Fig. 2). Source D (a Be star) is a strong H- α emitter (Herbig 1957) and has a disk (resolved by a radio image), similar to proplyds in the Orion nebula (O’Dell 2001). The component D is much fainter in X-rays than component C.

3.1. HD 164492A

The X-ray light curve of the HD164492A shows small but significant variability ($\sim 20\%$ in the 10 hour observation, Figure 4). This is unusual since most OB stars are not known X-ray variables. X-ray variability is not widely known from early type stars based on previous *Einstein* and *ROSAT* surveys (Chlebowski et al. 1989; Berghöfer et al. 1996). However, recent *Chandra* observations show significant variability from some early type stars (Feigelson et al. 2002). For example, θ^2 OriA, an O9.5 star, shows a 50% drop in 10 hr with multiple 10-20% flares (Feigelson et al. 2002). Some level of time variability is also observed from other early type stars in Orion (Schulz et al. 2001). The spectrum of the O star shows thermal emission as shown in Fig. 3a. We fit the X-ray spectra of HD164492A using two collisional ionization equilibrium (CIE) thermal models (a Mewe-Kaastra plasma model (Kaastra 1992) and an updated Raymond-Smith model (Raymond & Smith 1977); MEKAL and APEC in XSPEC). Both models gave similar results. We assumed sub-solar metal abundance (0.3 solar); assuming solar abundances produced less than a 20% change in the derived spectral parameters. The best fit of the spectrum of O star yields $N_H = 1(< 5) \times 10^{21} \text{ cm}^{-2}$ and a temperature of $kT_s = 0.5(< 0.6) \text{ keV}$, which implies an X-ray luminosity of $2.8 \times 10^{31} \text{ erg s}^{-1}$. The derived temperature is similar to the X-ray temperatures of other single massive stars (Corcoran et al. 1994; Moffat et al. 2002). Although some of the luminosity may be due to an unresolved low-mass companion such as a T-Tauri star which could be responsible for the variability, the low temperature obtained from the spectral fit is largely consistent with a single massive star. Assuming a bolometric luminosity of $L_{bol} \sim 0.5\text{--}1.6 \times 10^{39} \text{ ergs s}^{-1}$, the ratio of X-ray to bolometric luminosity is $-7.76 < \log L_x/L_{bol} < -7.25$, which is smaller than the canonical value $L_x/L_{bol} \approx -7$ but it is within the scatter (Berghöfer et al. 1996). The lack of high temperature X-

ray emission in HD164492A suggests that a magnetically confined wind shock has not developed in the O star of HD164492A as has been suggested in other variable O stars showing high temperature X-ray emission (like θ Ori A, C, and E Schulz et al. (2001)). Similarly the lack of hard emission in HD164492A also suggests that colliding wind emission (as considered in Rho et al. (2001)) is not important. X-rays from HD164492A are likely produced by shocks distributed through the star’s massive stellar wind. The variability may be from instabilities within a radiatively driven wind (Lucy & White 1980; Feldmeier et al. 1997), but if so the rapid timescale of the changes (~ 2 hours) suggests that the X-ray emission is dominated by a small number of strong shocks rather than a large distribution of weak shocks.

3.2. HD164492C

We also modelled the extracted spectrum from source C, which is blended with the unidentified X-ray source to the NW (source 91: Component C2) which is barely resolved from source C. The component D, a Be star, is not identified as a source by wavelet analysis; however, there is some faint X-ray emission coinciding with the Be star as shown in Figure 2. Component C2 (source 91) shows variability, and the light curve is shown in Fig. 4. The best two-temperature absorbed thermal fit in Fig. 3b has $N_H(1) = 7.8^{+5.2}_{-4.8} \times 10^{21} \text{ cm}^{-2}$ and a temperature of $kT_1 = 0.6 \pm 0.4 \text{ keV}$, and $N_H(2) = 1.6^{(+4.4)}_{(-1.1)} \times 10^{21} \text{ cm}^{-2}$ and a temperature of $kT_2 = 5.9^{(+\infty)}_{(-3.4)} \text{ keV}$. The luminosity of soft and hard components are 1.4×10^{32} and $6 \times 10^{31} \text{ erg s}^{-1}$, respectively. The lower absorption $N_H(1) = 1.6 \times 10^{21} \text{ cm}^{-2}$ is comparable to the optical extinction $A_v = 1 \text{ mag}$ (Kohoutek et al. 1999), suggesting that the wind(s) and the strong ionizing radiation from the O and B stars strip the surrounding materials. The 6 keV component is partially responsible for the spectra seen by *ASCA* (Rho et al. 2001). The X-ray emission from B and Be stars is not well characterized at present since they are often faint. The L_x/L_{Bol} ratio is below $10^{-7} \sim 10^{-5}$ for stars of spectral type B1.5(III-V) and later (Feigelson et al. 2002), and the late type stars have a luminosity range of 10^{29} - $10^{31} \text{ erg s}^{-1}$. Thus the observed X-ray emission of $2 \times 10^{32} \text{ erg s}^{-1}$ from the source C blend is difficult to reconcile with emission from a typical B6V type star or a late type main-sequence companion star. We extracted separate spectra from both components C and C2, but the spectra could not be distinguished from each other and additionally we lose the hard component emission due to lack of photon statistics in the hard energy band, although separate light curves show stronger time variability in the component C2. The B6V star is an X-ray source as shown in Figure 2, and the component C2 is a companion candidate which is also strong X-ray emitter. The companions of later B-type stars with strong X-ray emission, are suggested to be often PMS (Stelzer et al. 2003), which show characteristics of high X-ray luminosities and hard X-rays. The presence of an unidentified X-ray source near the B6V star and the presence of hard X-ray emission in this system suggest that C2 may be a PMS. Other possibilities such as emission from corona of the Herbig Be star, or a mechanism related to the proplyds remain open at this point.

3.3. HD 164492B

Component B (source 106) is classified as A2Ia (Gahm et al. 1983) or possibly as an A2 III (Lindroos 1985). A-type stars are not often detected as X-ray sources (Guillout et al. 1999) since they lack subsurface convection zones to power strong magnetic fields, and they lack a strong UV flux to power massive stellar winds. This may indicate that this star has a low-mass, X-ray bright companion or the spectral type may be incorrect. Its X-ray luminosity is listed in Table 2; we assumed a temperature of 0.15 keV from other A stars (Simon & Drake, 1993) and the absorption of $1.6 \times 10^{21} \text{ cm}^{-2}$.

4. Pre-main Sequence star candidates

We created lightcurves for each of the detected X-ray sources, using a bin length of 2500 sec, which gives a total number of 24 bins. We calculated the ratio between max count in the highest bin and minimum count in the lowest bin and found ~ 40 sources have the ratio greater than 1 after accounting for the errors. If a source was only detected during a flare, we used the mean count rate instead of minimum count rate.

In Table 2 we list sources in which this ratio greater than 3 (sources 8, 23, 97, 166, 170, 194, 211, 237, 246, 256, 283 and 285). These sources should represent the most strongly variable sources. To confirm this variability we also performed a simple χ^2 test against an assumed the constant light curve. The probability of constancy for each source from this test is given in Table 2, for which we used additional binning as needed for each source. Nine sources (sources 23, 91, 97, 166, 194, 237, 256, 283 and 285) in Table 2 are definitely variable (null probability $< 10\%$) based on the χ^2 test and our ratio test. We show sample light curves of the variable sources in Fig. 4.

We searched for near-infrared and optical counterparts for these variable sources. Unfortunately no previous optical identification of T Tauri stars exists in the Trifid. The only identified T Tauri stars or young stellar objects are 85 PMS candidates identified from infrared excesses using 2MASS second release data (Rho et al. 2001). Here we re-evaluate the identification of PMS candidates –TTS or YSO– from near-infrared color-color diagrams using the 2MASS final release data. The final release data have improved photometry by allowing multiple-components of point spread function for the blended sources with the improved zero point, and a complete source catalog by thoroughly identifying artifacts. Among variable sources in Table 2, only source 283 was previously identified as a YSO (Rho et al. 2001) and now sources 23, 97, 166, 194 and 237 are identified as TTS or YSO based on the 2MASS data. We also searched for optical counterparts to these X-ray sources using the Guide star catalog (GSC 2.2) and USNO-B catalog, but since these catalogs do not include any sources near bright optical diffuse emission, we also directly compared the X-ray sources in Table 1 to digital all sky images (DPOSS). Among the variable sources listed in Table 2, five (source 97, 166, 237, 256 and 285) have $\text{SHR} > -0.2$ (and they appear blue in Figure 1).

Sources 8, 23, 194, 211, 246 and 283 have both optical and 2MASS counterparts. These sources are not embedded and thus are likely in later stage of PMS evolution, possibly Class II or III. Sources 8, 211 and 246 have 2MASS counterparts, but not identified as TTS or YSO from near-infrared colors. They are still likely PMS, because the near-IR excess is shown to be time-dependent (Carpenter et al. 2000). Sources 97, 166, 237, 256 and 285 have no optical counterparts and have $\text{SHR} > -0.2$ and the light curve of source 166 is shown in Fig. 4. In particular, source 256 and 285 have neither near-IR nor optical counterparts but exhibit flares in their X-ray light curves as shown in Fig. 4. No radio counterparts are known for these sources. We suggest these X-ray flare stars are in an early pre-main sequence stage (Class I or earlier). Source 211 has sufficient counts for spectral fitting, and the best-fit using a one-temperature thermal model yields $N_H = 1(< 8) \times 10^{21} \text{ cm}^{-2}$ and a temperature of $kT = 2 (> 1) \text{ keV}$. The inferred X-ray luminosity of $1.1 \times 10^{31} \text{ erg s}^{-1}$, is comparable to those from TTS and YSO (Feigelson et al. 1999), and brighter than those of typical low-mass main-sequence stars ($\sim 10^{30} \text{ erg s}^{-1}$). The sources with flares seem to be found preferentially concentrated along the dust lane and at the edge of the HII region, i.e. along the ionization fronts. This reinforces the conclusion that most of flaring sources are PMS. We estimated the X-ray luminosities of sources 8, 23, 97, 166, 170, 194, 246, 256 and 283 assuming the spectral parameters are the same as those of source 211. For sources 237 and 285, we assumed the spectral parameters are the same as those of TC1 source, because their hardness ratios are comparable to that of TC1.

5. Identification of X-ray Emission from Massive Protostellar Cores

We compared the X-ray sources with the known massive star forming cores detected in the $1300\mu\text{m}$ dust continuum map (Lefloch et al. 2001). There are five such cores, four of which are known to have bipolar wings. We detected X-ray emission from TC1 (source 117) and possibly TC4 (source 38), two cores with bipolar wings and associated Class 0 candidates (Cernicharo et al. 1998; Lefloch & Cernicharo 2000). The sources associated with both TC1 and TC4 are hard X-ray sources (which appear as blue sources in Figure 1). Figure 5 shows the positions of the X-ray sources superposed on the $1300\mu\text{m}$ dust continuum map. The X-ray source associated with TC1 has no 2MASS counterpart. But the X-ray identification of the source associated with the TC4 core is less clear, because this source is located at the edge of the ACIS field of view where the width of PSF is $\sim 12''$. The TC4 source coincides with the $1300\mu\text{m}$ dust continuum source within $11 - 12''$, and also has two 2MASS counterparts within $12''$. The closest 2MASS source is 2MASS180212.5-230549 for which J band emission is not detected and $H(=14.8\text{mag})$ and $K_s(=12.9\text{mag})$ magnitudes are contaminated by a nearby star. It is not clear if this 2MASS source is related to the TC4 and the X-ray source. TC4 satisfies the Class 0 definition of Andre et al. (1993) in terms of its dust temperature ($\sim 20 \text{ K}$), the ratio of its submillimeter to bolometric luminosity, and the presence of a bipolar outflow. An outflow from TC4 shows a kinematic age of $6.8 \times 10^3 \text{ yr}$ and suggests it to be an intermediate- or high-mass object (Lefloch et al. 2002). For TC1, the SED is not available so it's not clear if TC1 satisfies the Class 0 criteria or not; however, the object is

deeply embedded in a dust core so it is at least a Class I object, and possibly younger than a Class I source.

TC1 and TC4 have hardness ratios of 0.24 and 0.67, respectively (see Table 1 and 2). The source associated with TC4 is one of the hardest sources in Table 1. These sources are either highly absorbed or have high temperatures. Our analysis of the X-ray spectra of TC1 and TC4 shows that the best fit thermal model parameters are $N_H = 6 \times 10^{22} \text{ cm}^{-2}$, $kT = 1.7 \text{ keV}$ and $L_x = 4.7 \times 10^{31} \text{ erg s}^{-1}$ for the TC 4 source, and $N_H = 3.4 \times 10^{22} \text{ cm}^{-2}$, $kT = 1.1 \text{ keV}$, and $L_x = 1.9 \times 10^{31} \text{ erg s}^{-1}$ for the TC1 source. The large column densities we derive show that these sources are highly embedded. The only detection of X-ray emission from a Class 0 object until now is a source located in OMC-3 (CSO6) (Tsuboi et al. 2001). In comparison, the Class 0 source in OMC-3 (CSO6) has $N_H = (1 - 3) \times 10^{23} \text{ cm}^{-2}$ and a luminosity of $10^{30} \text{ erg s}^{-1}$. X-ray emission from Class 0 objects which are in the dynamical infall phase is poorly understood since so far only a few Class 0 candidates have been identified and their properties are not well constrained. It is unclear if the X-ray emission is due to solar-type magnetic activities as in Class I objects. The fact that these two counterparts have high hardness ratios does not support the X-ray emission is from a low-mass companion to the protostellar core. If these objects are accreting, then the X-ray emission may be related to the accumulation and release of angular momentum toward the growing central star by outflow processes.

6. Summary

Young HII regions like the Trifid are rich sources of X-ray emitters. Our *Chandra* images reveal a few hundred X-ray sources including variable and hard sources, along with pre-main sequence stars and more evolved OB stars. We summarize our findings here.

1. *Chandra* images show 304 X-ray sources; thirty percent of the sources are hard, and two-thirds have near-infrared counterparts. The full list of *Chandra* X-ray sources is given in Table 1.

2. The multiple star system HD164492 is resolved for the first time in X-rays into individual components. X-ray emission is detected from components A, B, C (a B6V star), which is blended with an unidentified source in the *Chandra* images. This blend has comparable X-ray brightness to the O star. The O star HD 164492A shows small but significant variability and has a soft spectrum with a temperature of 0.5 keV. The temperature is comparable to those of other single massive stars and the ratio of X-ray and bolometric luminosities is smaller than the canonical value $L_x/L_{bol} \approx -7$ but it is within the scatter of distribution. The lack of any hard component suggests that neither a magnetically confined wind shock nor colliding wind shock is needed to describe the X-ray emission from the O star. The variability of the X-ray emission implies that the emission is produced by a small number of strong shocks in the wind of HD 164492A.

3. The X-ray spectrum from the component C blend requires a two-temperature thermal model

with $kT_1 = 0.6 \pm 0.4$ keV and $kT_2 = 5.9^{(+\infty)}_{(-3.4)}$ keV. The inferred X-ray luminosity is 2×10^{32} erg s $^{-1}$. This blend is highly variable in X-rays which suggests that one of the stars dominates the emission.

4. We found a dozen stars which show evidence of flaring activity and there could be many as ~ 40 variable stars in the full source list. Nine sources (sources 8, 23, 97, 166, 194, 237, 256, 283 and 285 in Table 2) have significant variability based on the χ^2 statistics. We searched for their near-infrared and optical counterparts, and found that six stars have both optical and 2MASS counterparts. These sources are likely in later stages of PMS evolution. Four sources which have no optical counterparts and have SHR greater than -0.2 are likely in early stages of PMS, possibly Class I or earlier. There are a few stars with neither near-IR nor optical counterpart whose light curves show strong flares, suggesting that they are very early stage pre-main sequence stars.

5. We detected X-ray emission from TC1 and possibly TC4, two massive star forming cores with bipolar wings and associated Class 0 candidates. Both TC1 and TC4 show extremely hard X-rays and their spectra imply very high absorption ($N_H = 3.5 - 6 \times 10^{22}$ cm $^{-2}$) and high luminosity ($2 - 5 \times 10^{31}$ erg s $^{-1}$). Only one other detection of X-ray emission from a Class 0 object has been previously reported. Thus our two detections imply the second and third X-ray detection of a Class 0 object. It is unclear if the X-ray emission of these objects is due to solar-type magnetic activities as in Class I objects. If the X-ray emission is from the accreting stage, the X-ray emission may be related to the competing processes of accumulation of angular momentum toward the growing central star and release of angular momentum by outflow processes.

Thirty percent of the X-ray sources in the full field are shown to be hard (SHR > -0.2) sources (shown in blue in Figure 1), and 16 percent of sources are extremely hard sources (SHR $> +0.2$). A high proportion of these sources are probably PMS because they are either highly embedded or extremely high temperature. These hard sources along with the sources near HD 164492C are responsible for the hard spectra seen by *ASCA*. The accurate positions from the complete list of the X-ray sources are provided in Table 1. These sources provide an opportunity to identify interesting PMS using the multi-wavelength follow-up observations, which will help us to further understand the population and evolution of protostellar objects.

Partial support for this work was provided by NASA through *Chandra* grant G02-3095A. J. R. and S. V. R. acknowledge the support of California Institute of Technology, the Jet Propulsion Laboratory, which is operated under contract with NASA.

REFERENCES

- Abbott, D. C., 1982, ApJ, 263, 723
- Andre, P., Ward-Thompson, D., & Barsony, M., 1993, ApJ, 406, 122-141
- Berghöfer, T. W., Schmitt, J. H. M. M., & Cassinelli, J. P., 1996, A&AS, 118, 481
- Carpenter, J. M., Hillenbrand, L.A. & Skrutskie, M. F., 2001, AJ, 121, 3160
- Cassinelli, J. P. & Cohen, D. H., 1994, IAUS, *Pulsation, rotation and mass loss in early-type stars* (Kluwer Academic Publishers), 162, 189
- Cernicharo et al. 1998, Science, 282, 462 (CLC98)
- Chlebowski, T., Harnden, F. R., & Sciortino, S. 1989, ApJ, 341, 427
- Corcoran, M. F., et al., 1994; ApJ, 436, L95
- Feigelson, E. D., Broos, P., Gaffney, J. A., Garmire, G., Hillenbrand, L. A., Pravdo, S. H., Townsley, L., & Tsuboi, Y., 2002, ApJ, 574, 258-292
- Feigelson, E. D., & Montmerle, T., 1999, ARA&A, 37, 363
- Feldmeier, A., Kudritzki, R. P., Palsa, R., Pauldrach, A.W.A., Puls, J., 1997, ApJ, 320, 899
- Freeman, P. E., Kashyap, V., Rosner, R., & Lamb, D. Q., 2002, ApJS, 138, 185
- Gahm, G. F., Ahlin, P., Lindroos, K. P., 1983, A&AS, 51, 143
- Garmire et al., 2000, AJ, 120, 1426
- Guillout, P., Schmitt, J. H. M. M., Egret, D., Voges, W., Motch, C., & Sterzik, M. F. 1999, A&A, 351, 1003
- Herbig, G. H., 1957, ApJ, 125, 654
- Hester et al, 1999, BAAS, 194.681
- Imanishi, K., Koyama, K., & Tsuboi, Y., 2001, ApJ, 557, 747
- Kaastra, J. S. 1992, An X-ray Spectral Code for Optically Thin Plasmas (SRON-Leiden Report)
- Kohoutek, L., Mayer, Pl, & Lorenz, R., 1999, A &AS, 134, 129
- Kohn, L., Koyama, K., & Hamaguchi, K., 2002, ApJ, 567, 423
- Lada, C. J., 1987, IAU Symp. 115: Star Forming Regions, p.1-15
- Lefloch, B. & Cernicharo, J., 2000, ApJ, 545, 340

- Lefloch, B., Cernicharo, J., Cesarsky, D., Demyk, K., & Rodríguez, L.F., 2001, A&A, 368, L13
- Lefloch, B., Cernicharo, J., Rodríguez, L.F., Miville-Deschenes, M.A., & Cesarsky, D., 2002, ApJ, 581, 335
- Lindroos, K. P. 1985, A&AS, 60, 183L
- Lucy, L. B., & White, R. L., ApJ, 1980, 241, 300
- Lynds, B. T., & O’Neil, E. J., Jr., 1985, ApJ, 294, 578
- Moffat., A.J, Corcoran, M., et al., 2002, ApJ, 573, 191
- O’Dell, C.R., 2001, ApJ, 122, 2662
- Raymond, J.C. and Smith, B.W., 1977, ApJS, 35, 419
- Rho, J., Corcoran, M.F, Chu, Y.-H., & Reach, W. T., 2001, ApJ, 562, 446
- Schulz, N.S, Canizares, C., Huenemoerder, D., Kastner, J.H., Taylor, S.C., & Bergstrom, E. J., 2001, ApJ, 549, 441
- Simon, T. & Drake, S. A., 1993, AJ, 106, 1660
- Stelzer, B., Huélamo, N., Hubrig, S., Zinnercker, H., & Micela, G., 2003, A&A, 407, 1067
- Townsley, L. K., Broos, P. S., Garmire, G. P., & Nousek, J. A., 2000, ApJ, 534, 139L
- Townsley, L. K., Feigelson, E. D., Montmerld, T., Broos, P. S., Chu, Y.-H., & Garmire, G. P., 2003, ApJ, 593, 874
- Tsuboi, Y., Koyama, K., Hamaguchi, K., Tatematsu, K., Sekimoto, Y., Bally, J., & Reipurth, B. 2001, ApJ, 554, 734
- Weisskopf, M. C., Brinkman, B., Canizares, C., Garmire, G., Murray, S., & Van Speybroeck, L. P., 2002, PASP, 114, 1

Table 1. Catalog of X-ray sources

No	WID	CXOM20	Net Counts cts ks ⁻¹	SNR	Hardness Ratio
1	177	18:01:50.61–22:54:39.6	12 ± 4	3	-0.23 ± 0.20
2	208	18:01:50.79–22:52:18.5	22 ± 7	3	0.09 ± 0.13
3	206	18:01:52.54–22:57:33.6	22 ± 6	4	-0.26 ± 0.16
4	207	18:01:53.57–22:51:35.6	24 ± 7	4	0.56 ± 0.16
5	333	18:01:57.18–23:01:22.1	58 ± 9	11	-0.49 ± 0.14
6	344	18:01:57.64–23:00:01.7	13 ± 4	3	-0.19 ± 0.20
7	197	18:01:58.33–22:52:26.5	21 ± 6	5	-0.36 ± 0.14
8	196	18:01:59.07–22:52:27.5	73 ± 10	12	-0.49 ± 0.11
9	352	18:01:59.12–23:00:55.3	20 ± 5	5	0.76 ± 0.22
10	195	18:01:59.85–22:53:14.8	41 ± 7	9	-0.62 ± 0.16
11	203	18:02:02.04–22:54:19.1	14 ± 4	4	-0.36 ± 0.23
12	348	18:02:02.07–23:00:56.2	13 ± 4	4	0.69 ± 0.10
13	332	18:02:02.54–23:02:32.5	103 ± 11	20	0.81 ± 0.12
14	343	18:02:03.13–22:59:09.6	13 ± 4	4	-0.33 ± 0.19
15	201	18:02:03.45–22:56:07.2	13 ± 4	4	-0.69 ± 0.34
16	194	18:02:03.86–22:52:58.0	45 ± 7	10	0.84 ± 0.18
17	313	18:02:04.75–23:04:03.0	11 ± 4	3	0.29 ± 0.19
18	189	18:02:05.50–22:55:01.2	19 ± 5	6	-0.65 ± 0.25
19	341	18:02:06.05–23:00:49.9	14 ± 4	4	-0.60 ± 0.30
20	175	18:02:07.02–22:57:25.8	13 ± 4	6	-0.53 ± 0.27
21	174	18:02:07.62–22:57:42.7	102 ± 10	37	-0.51 ± 0.11
22	188	18:02:07.75–22:57:23.4	22 ± 5	8	0.92 ± 0.28
23	173	18:02:07.77–22:55:33.9	58 ± 8	19	-0.58 ± 0.15
24	172	18:02:08.09–22:57:18.6	39 ± 6	14	-0.85 ± 0.21
25	289	18:02:08.52–22:59:00.0	62 ± 8	24	-0.76 ± 0.15
26	354	18:02:09.18–23:02:36.9	5 ± 2	2	0.00 ± 0.22
27	205	18:02:09.42–22:50:56.1	10 ± 4	3	-0.12 ± 0.20
28	339	18:02:09.92–23:04:27.5	43 ± 8	8	-0.47 ± 0.15
29	186	18:02:10.46–22:55:13.8	28 ± 5	11	-0.66 ± 0.22
30	185	18:02:10.80–22:55:32.6	14 ± 4	6	-0.25 ± 0.26
31	353	18:02:11.27–23:04:11.9	18 ± 5	4	0.14 ± 0.17
32	160	18:02:11.36–22:56:50.8	74 ± 9	29	-0.53 ± 0.13

Table 1—Continued

No	WID	CXOM20	Net Counts cts ks ⁻¹	SNR	Hardness Ratio
33	246	18:02:11.63–22:59:33.9	189 ± 14	70	-0.54 ± 0.08
34	204	18:02:11.66–22:50:10.8	21 ± 6	4	0.31 ± 0.19
35	170	18:02:11.78–22:56:45.8	34 ± 6	14	0.24 ± 0.18
36	159	18:02:11.95–22:55:43.6	294 ± 17	92	-0.70 ± 0.07
37	351	18:02:12.26–23:03:10.4	14 ± 4	3	0.33 ± 0.22
38	347	18:02:12.47–23:05:48.1	62 ± 9	9	0.67 ± 0.13
39	311	18:02:12.68–22:58:52.2	6 ± 2	2	1.00 ± 0.45
40	199	18:02:12.79–22:57:00.0	6 ± 3	3	0.80 ± 0.40
41	288	18:02:13.15–23:01:59.3	92 ± 10	27	-0.66 ± 0.12
42	338	18:02:13.38–23:04:13.5	9 ± 4	3	0.38 ± 0.27
43	192	18:02:13.50–22:57:31.4	6 ± 2	2	0.00 ± 0.35
44	287	18:02:13.83–22:58:36.1	30 ± 6	13	-0.69 ± 0.21
45	286	18:02:13.95–23:02:12.7	115 ± 11	29	-0.23 ± 0.09
46	168	18:02:14.37–22:54:21.5	55 ± 7	22	-0.75 ± 0.17
47	285	18:02:15.56–23:02:22.5	47 ± 7	14	-0.49 ± 0.15
48	350	18:02:15.79–23:05:56.1	20 ± 6	4	-0.43 ± 0.14
49	284	18:02:15.85–22:58:27.4	14 ± 4	6	-0.60 ± 0.30
50	167	18:02:16.17–22:57:23.4	9 ± 3	4	-1.00 ± 0.47
51	244	18:02:16.44–22:59:39.5	36 ± 6	15	-0.78 ± 0.21
52	283	18:02:16.61–22:58:36.8	11 ± 3	5	-0.67 ± 0.35
53	282	18:02:16.81–23:03:47.0	167 ± 14	31	-0.63 ± 0.09
54	280	18:02:17.01–22:59:17.8	13 ± 4	6	-1.00 ± 0.41
55	279	18:02:17.28–22:57:50.9	22 ± 5	10	0.91 ± 0.28
56	202	18:02:17.36–22:53:44.6	7 ± 3	3	-0.56 ± 0.38
57	156	18:02:17.65–22:56:18.0	26 ± 5	12	-0.85 ± 0.26
58	310	18:02:17.91–23:04:07.3	10 ± 4	3	-0.67 ± 0.35
59	309	18:02:17.97–23:00:14.0	9 ± 3	4	-0.82 ± 0.39
60	331	18:02:18.18–23:03:43.4	30 ± 6	8	-0.89 ± 0.22
61	337	18:02:18.78–23:03:42.4	37 ± 7	10	-0.57 ± 0.17
62	198	18:02:18.90–22:51:45.1	26 ± 6	7	-0.66 ± 0.20
63	336	18:02:19.09–23:03:32.7	11 ± 4	3	0.00 ± 0.24
64	155	18:02:19.17–22:53:46.3	97 ± 10	34	-0.77 ± 0.13

Table 1—Continued

No	WID	CXOM20	Net Counts cts ks ⁻¹	SNR	Hardness Ratio
65	243	18:02:19.19–22:58:36.7	15 ± 4	6	-0.60 ± 0.30
66	242	18:02:19.70–22:59:40.6	11 ± 3	5	-1.00 ± 0.45
67	278	18:02:19.98–23:01:21.3	17 ± 4	7	-0.14 ± 0.22
68	330	18:02:20.43–23:03:15.7	18 ± 5	5	0.68 ± 0.24
69	165	18:02:20.57–22:53:56.2	18 ± 4	7	-0.37 ± 0.24
70	346	18:02:20.76–23:02:41.1	15 ± 4	4	-0.08 ± 0.20
71	329	18:02:21.05–22:59:02.5	6 ± 2	2	-1.00 ± 0.53
72	308	18:02:21.06–23:01:43.6	40 ± 7	12	-0.45 ± 0.17
73	241	18:02:21.07–23:03:13.9	507 ± 23	97	-0.51 ± 0.05
74	328	18:02:21.20–23:00:17.3	3 ± 2	1	0.33 ± 0.61
75	240	18:02:21.26–22:57:50.1	54 ± 7	21	-0.53 ± 0.16
76	335	18:02:21.27–23:01:28.8	9 ± 3	3	-0.57 ± 0.31
77	239	18:02:21.46–23:01:02.5	66 ± 8	23	-0.55 ± 0.14
78	238	18:02:21.93–23:00:57.7	114 ± 11	39	-0.72 ± 0.12
79	307	18:02:21.96–23:02:07.2	31 ± 6	8	-0.38 ± 0.17
80	190	18:02:22.04–22:54:15.7	9 ± 3	4	-0.64 ± 0.36
81	277	18:02:22.24–23:01:50.5	38 ± 7	8	-0.44 ± 0.15
82	306	18:02:22.27–23:00:46.4	14 ± 4	6	-0.76 ± 0.31
83	049	18:02:22.36–22:49:09.3	41 ± 8	7	0.68 ± 0.16
84	179	18:02:22.36–22:56:35.2	9 ± 3	4	0.20 ± 0.32
85	276	18:02:22.42–23:02:10.7	80 ± 9	18	-0.67 ± 0.13
86	275	18:02:22.61–23:01:58.9	116 ± 12	20	-0.41 ± 0.09
87	305	18:02:22.78–23:00:18.5	7 ± 3	3	1.00 ± 0.45
88	327	18:02:22.81–23:01:52.3	5 ± 3	1	-0.67 ± 0.25
89	237	18:02:22.86–22:59:35.6	29 ± 5	12	-0.03 ± 0.19
90	274	18:02:22.90–23:01:28.5	35 ± 6	10	-0.12 ± 0.15
91	235	18:02:23.05–23:01:58.1	857 ± 30	129	-0.47 ± 0.03
92	273	18:02:23.06–23:01:25.3	8 ± 3	3	-0.64 ± 0.36
93	236	18:02:23.09–23:01:44.8	317 ± 18	52	-0.63 ± 0.06
94	234	18:02:23.16–23:02:00.3	831 ± 29	119	-0.50 ± 0.03
95	304	18:02:23.19–23:00:23.6	9 ± 3	4	-0.69 ± 0.34
96	233	18:02:23.21–23:00:12.3	17 ± 4	7	-0.58 ± 0.27

Table 1—Continued

No	WID	CXOM20	Net Counts cts ks ⁻¹	SNR	Hardness Ratio
97	272	18:02:23.25–23:01:35.0	48 ± 7	12	-0.18 ± 0.13
98	303	18:02:23.32–23:03:11.3	20 ± 5	6	0.00 ± 0.20
99	232	18:02:23.41–23:01:41.5	90 ± 10	20	-0.75 ± 0.11
100	326	18:02:23.41–23:02:22.4	19 ± 5	5	-0.71 ± 0.23
101	231	18:02:23.51–23:00:23.3	65 ± 8	25	-0.13 ± 0.12
102	230	18:02:23.54–23:01:50.9	884 ± 30	114	-0.89 ± 0.04
103	270	18:02:23.63–23:03:27.7	155 ± 13	33	-0.18 ± 0.08
104	268	18:02:23.65–23:00:55.6	40 ± 6	15	-0.29 ± 0.16
105	269	18:02:23.66–23:01:57.3	35 ± 7	8	-0.60 ± 0.16
106	229	18:02:23.71–23:01:45.4	299 ± 18	47	-0.64 ± 0.07
107	267	18:02:23.83–22:59:39.0	21 ± 5	9	-0.45 ± 0.23
108	164	18:02:23.95–22:54:30.7	23 ± 5	10	-0.67 ± 0.22
109	302	18:02:23.98–23:04:19.2	204 ± 15	35	-0.51 ± 0.08
110	301	18:02:24.17–23:00:36.6	7 ± 3	3	-0.80 ± 0.40
111	020	18:02:24.19–22:51:13.2	12 ± 4	4	-0.87 ± 0.34
112	228	18:02:24.29–22:59:27.1	72 ± 9	30	-0.75 ± 0.15
113	266	18:02:24.57–23:00:20.7	20 ± 5	8	-0.24 ± 0.22
114	227	18:02:24.63–23:01:03.7	76 ± 9	26	0.26 ± 0.12
115	154	18:02:24.90–22:55:26.4	18 ± 4	8	-0.89 ± 0.31
116	265	18:02:25.12–23:02:17.4	79 ± 9	23	-0.76 ± 0.14
117	264	18:02:25.16–23:01:26.7	41 ± 7	15	0.24 ± 0.16
118	010	18:02:25.17–22:53:41.0	14 ± 4	6	-0.47 ± 0.28
119	323	18:02:25.34–23:03:55.5	83 ± 10	17	-0.56 ± 0.13
120	324	18:02:25.35–23:02:56.7	32 ± 6	9	-0.57 ± 0.19
121	226	18:02:25.37–23:00:36.3	25 ± 5	10	-0.77 ± 0.25
122	300	18:02:25.43–23:01:39.9	27 ± 5	9	-0.47 ± 0.20
123	262	18:02:25.63–23:00:56.9	50 ± 7	19	-0.37 ± 0.15
124	261	18:02:25.84–23:01:42.6	25 ± 5	9	-0.61 ± 0.21
125	225	18:02:25.93–23:00:11.6	69 ± 8	28	-0.67 ± 0.10
126	224	18:02:25.94–23:00:34.6	87 ± 9	33	-0.57 ± 0.12
127	260	18:02:25.95–22:58:03.2	16 ± 4	7	0.05 ± 0.23
128	223	18:02:25.99–23:00:13.4	170 ± 13	62	-0.77 ± 0.09

Table 1—Continued

No	WID	CXOM20	Net Counts cts ks ⁻¹	SNR	Hardness Ratio
129	178	18:02:25.99–22:55:27.8	4 ± 2	2	-0.20 ± 0.46
130	259	18:02:26.01–23:02:27.7	61 ± 8	19	-0.60 ± 0.14
131	258	18:02:26.09–23:01:28.6	5 ± 2	2	-1.00 ± 0.63
132	321	18:02:26.47–23:01:55.9	16 ± 4	5	-0.40 ± 0.24
133	222	18:02:26.85–23:00:14.3	61 ± 8	24	-0.48 ± 0.14
134	019	18:02:26.95–22:51:07.9	108 ± 11	25	-0.68 ± 0.11
135	256	18:02:27.13–23:00:50.6	9 ± 3	4	-0.09 ± 0.30
136	255	18:02:27.17–23:03:33.4	215 ± 15	45	-0.75 ± 0.08
137	220	18:02:27.32–22:59:37.7	34 ± 6	14	-0.71 ± 0.21
138	349	18:02:27.45–23:04:13.7	17 ± 5	4	-0.56 ± 0.20
139	299	18:02:27.56–23:00:20.3	8 ± 3	3	-0.56 ± 0.38
140	254	18:02:27.97–22:58:56.9	11 ± 3	5	-0.82 ± 0.39
141	298	18:02:28.03–23:01:43.0	19 ± 5	6	-0.39 ± 0.22
142	320	18:02:28.13–23:02:11.1	11 ± 4	4	-0.75 ± 0.31
143	253	18:02:28.41–22:59:47.3	25 ± 5	10	-0.54 ± 0.22
144	004	18:02:28.44–22:55:44.5	21 ± 5	9	-1.00 ± 0.32
145	319	18:02:28.44–23:01:14.1	11 ± 3	4	-0.69 ± 0.34
146	219	18:02:28.51–23:00:37.7	297 ± 17	95	-0.36 ± 0.06
147	297	18:02:28.52–23:00:14.6	7 ± 3	3	1.00 ± 0.45
148	048	18:02:28.54–22:51:45.8	13 ± 4	4	-0.39 ± 0.22
149	218	18:02:28.65–23:03:03.4	432 ± 21	86	-0.53 ± 0.05
150	318	18:02:28.66–23:01:36.8	6 ± 3	2	-0.25 ± 0.26
151	217	18:02:28.74–22:59:47.4	269 ± 16	91	-0.62 ± 0.07
152	216	18:02:28.80–22:59:00.1	54 ± 7	22	-0.41 ± 0.15
153	317	18:02:28.81–23:02:25.5	21 ± 5	7	-0.89 ± 0.22
154	252	18:02:29.10–23:00:40.9	19 ± 4	8	0.20 ± 0.23
155	009	18:02:29.14–22:52:52.6	108 ± 11	32	-0.75 ± 0.12
156	215	18:02:29.35–23:01:01.6	29 ± 5	11	-0.47 ± 0.20
157	214	18:02:29.47–22:59:14.7	25 ± 5	11	-0.56 ± 0.22
158	018	18:02:29.53–22:55:36.5	13 ± 4	5	-0.73 ± 0.32
159	117	18:02:29.59–22:56:54.4	4 ± 2	2	-1.00 ± 0.71
160	213	18:02:29.60–22:58:59.3	16 ± 4	7	-0.50 ± 0.28

Table 1—Continued

No	WID	CXOM20	Net Counts cts ks ⁻¹	SNR	Hardness Ratio
161	040	18:02:29.68–22:50:12.5	14 ± 4	4	0.90 ± 0.29
162	003	18:02:29.79–22:56:03.5	24 ± 5	11	-0.67 ± 0.25
163	345	18:02:30.03–23:02:02.5	4 ± 2	1	1.00 ± 0.39
164	250	18:02:30.19–23:00:39.5	30 ± 6	12	0.44 ± 0.19
165	251	18:02:30.20–22:59:50.2	10 ± 3	4	-0.45 ± 0.33
166	212	18:02:30.37–22:59:29.1	135 ± 12	57	-0.19 ± 0.09
167	249	18:02:30.38–23:01:34.5	96 ± 10	30	-0.74 ± 0.12
168	053	18:02:30.47–22:48:58.6	40 ± 8	7	0.47 ± 0.14
169	032	18:02:30.89–22:53:03.8	16 ± 4	5	-0.79 ± 0.29
170	211	18:02:30.93–23:02:35.6	73 ± 9	21	-0.79 ± 0.15
171	210	18:02:30.98–23:00:43.6	128 ± 11	43	0.48 ± 0.10
172	316	18:02:31.10–23:00:31.5	9 ± 3	4	0.33 ± 0.30
173	296	18:02:31.20–23:01:24.4	36 ± 6	13	-0.45 ± 0.17
174	295	18:02:31.22–23:01:20.8	18 ± 4	7	-0.50 ± 0.21
175	294	18:02:31.55–23:01:49.4	28 ± 6	9	-0.71 ± 0.23
176	017	18:02:31.67–22:55:12.1	10 ± 3	4	0.45 ± 0.33
177	209	18:02:31.71–23:02:16.8	97 ± 10	30	-0.59 ± 0.11
178	315	18:02:31.82–23:03:33.9	13 ± 4	4	-0.65 ± 0.29
179	293	18:02:31.84–23:00:24.9	8 ± 3	3	-0.85 ± 0.36
180	096	18:02:31.89–22:58:02.0	7 ± 3	3	0.43 ± 0.41
181	140	18:02:31.94–23:00:24.7	5 ± 2	2	-0.83 ± 0.38
182	248	18:02:31.99–23:02:40.4	164 ± 13	38	-0.79 ± 0.10
183	016	18:02:32.00–22:53:59.8	15 ± 4	6	-0.18 ± 0.25
184	095	18:02:32.30–22:59:27.9	8 ± 3	3	-0.75 ± 0.44
185	314	18:02:32.38–23:04:54.8	40 ± 7	8	-0.42 ± 0.15
186	008	18:02:32.40–22:56:16.0	14 ± 4	6	0.86 ± 0.35
187	015	18:02:32.60–22:53:25.6	8 ± 3	4	-0.67 ± 0.35
188	292	18:02:32.61–23:01:16.4	21 ± 5	9	-0.82 ± 0.28
189	094	18:02:32.61–22:59:24.5	15 ± 4	7	-0.75 ± 0.31
190	132	18:02:32.63–22:59:37.6	10 ± 3	4	-0.27 ± 0.31
191	093	18:02:32.67–22:59:49.5	27 ± 5	11	-0.50 ± 0.21
192	116	18:02:32.68–22:59:46.3	14 ± 4	6	0.12 ± 0.25

Table 1—Continued

No	WID	CXOM20	Net Counts cts ks ⁻¹	SNR	Hardness Ratio
193	115	18:02:32.74–23:00:46.7	16 ± 4	7	-0.18 ± 0.25
194	291	18:02:32.75–23:04:21.0	74 ± 9	14	-0.58 ± 0.13
195	114	18:02:32.79–22:59:20.5	8 ± 3	3	1.00 ± 0.45
196	290	18:02:33.02–23:03:10.8	73 ± 9	18	0.83 ± 0.14
197	002	18:02:33.03–22:55:47.7	22 ± 5	9	0.13 ± 0.21
198	334	18:02:33.16–23:02:37.4	9 ± 3	3	-0.62 ± 0.29
199	092	18:02:33.34–23:01:11.3	9 ± 3	4	-0.54 ± 0.32
200	091	18:02:33.53–23:01:17.4	34 ± 6	13	-0.63 ± 0.19
201	113	18:02:33.67–22:59:54.3	9 ± 3	4	-1.00 ± 0.43
202	039	18:02:33.67–22:52:57.4	10 ± 3	3	1.00 ± 0.41
203	001	18:02:33.78–22:55:37.5	99 ± 10	40	-0.72 ± 0.12
204	074	18:02:33.78–22:58:40.9	24 ± 5	11	-0.92 ± 0.27
205	031	18:02:33.90–22:53:22.8	18 ± 4	7	-0.57 ± 0.22
206	090	18:02:33.91–22:59:52.6	25 ± 5	10	-0.04 ± 0.20
207	030	18:02:34.02–22:50:13.4	77 ± 10	15	-0.71 ± 0.13
208	247	18:02:34.03–23:03:17.9	182 ± 14	36	-0.50 ± 0.08
209	073	18:02:34.33–23:01:15.4	154 ± 13	47	-0.66 ± 0.10
210	112	18:02:34.45–22:58:10.8	11 ± 3	5	-0.23 ± 0.28
211	072	18:02:34.51–22:59:38.0	312 ± 18	107	-0.47 ± 0.06
212	071	18:02:34.57–23:00:30.9	45 ± 7	16	-0.32 ± 0.16
213	047	18:02:34.70–22:51:25.3	10 ± 4	3	0.14 ± 0.27
214	111	18:02:34.85–23:00:46.1	9 ± 3	4	1.00 ± 0.35
215	131	18:02:34.91–23:01:48.7	16 ± 4	5	0.14 ± 0.22
216	089	18:02:35.05–23:00:52.6	79 ± 9	28	-0.68 ± 0.13
217	110	18:02:35.24–23:01:02.3	10 ± 3	4	-0.20 ± 0.26
218	130	18:02:35.33–23:00:09.7	8 ± 3	3	-0.33 ± 0.35
219	070	18:02:35.55–22:59:55.5	92 ± 10	36	-0.74 ± 0.13
220	109	18:02:35.74–23:02:58.6	145 ± 12	35	-0.41 ± 0.09
221	088	18:02:35.95–22:59:47.0	21 ± 5	8	-0.70 ± 0.24
222	068	18:02:35.98–23:01:40.8	182 ± 14	52	-0.55 ± 0.08
223	057	18:02:36.07–22:49:39.5	14 ± 5	3	0.11 ± 0.17
224	108	18:02:36.09–22:59:19.9	8 ± 3	3	-0.11 ± 0.34

Table 1—Continued

No	WID	CXOM20	Net Counts cts ks ⁻¹	SNR	Hardness Ratio
225	087	18:02:36.11–23:01:31.9	60 ± 8	19	-0.78 ± 0.16
226	107	18:02:36.29–22:57:33.3	9 ± 3	4	-0.64 ± 0.36
227	067	18:02:36.45–22:59:59.6	24 ± 5	9	-0.76 ± 0.25
228	086	18:02:36.70–22:58:04.2	32 ± 6	13	-0.88 ± 0.23
229	066	18:02:36.81–23:00:24.0	48 ± 7	18	-0.65 ± 0.17
230	139	18:02:36.83–23:04:00.6	19 ± 5	6	-0.31 ± 0.18
231	151	18:02:36.92–23:04:14.8	16 ± 5	4	-0.48 ± 0.23
232	046	18:02:37.27–22:47:42.9	30 ± 7	5	-0.54 ± 0.13
233	129	18:02:37.33–23:01:04.1	11 ± 4	4	-0.69 ± 0.34
234	106	18:02:37.44–23:00:48.7	9 ± 3	4	-0.71 ± 0.33
235	128	18:02:37.76–23:02:11.9	10 ± 3	3	-0.85 ± 0.36
236	065	18:02:38.26–22:58:54.8	322 ± 18	121	-0.75 ± 0.07
237	029	18:02:38.85–22:50:06.1	81 ± 10	13	0.24 ± 0.09
238	045	18:02:38.94–22:50:21.0	22 ± 6	5	0.72 ± 0.21
239	127	18:02:39.03–22:59:50.5	13 ± 4	5	-0.20 ± 0.26
240	055	18:02:39.07–22:48:22.8	43 ± 9	6	-0.03 ± 0.11
241	104	18:02:39.59–23:03:44.0	87 ± 10	17	-0.53 ± 0.11
242	064	18:02:39.94–23:00:12.9	119 ± 11	43	-0.58 ± 0.11
243	103	18:02:40.11–23:01:45.8	23 ± 5	7	-0.70 ± 0.24
244	084	18:02:40.18–23:04:04.5	48 ± 8	11	0.84 ± 0.17
245	054	18:02:40.21–22:48:34.8	26 ± 7	4	-0.05 ± 0.11
246	063	18:02:40.42–22:57:53.3	58 ± 8	23	-0.86 ± 0.17
247	083	18:02:40.61–23:01:28.4	85 ± 9	26	-0.52 ± 0.12
248	014	18:02:40.66–22:55:17.5	14 ± 4	6	-0.71 ± 0.33
249	138	18:02:40.83–23:00:54.6	6 ± 3	2	0.45 ± 0.33
250	052	18:02:41.25–22:49:05.4	46 ± 8	7	-0.17 ± 0.09
251	082	18:02:41.25–23:01:14.0	110 ± 11	31	-0.61 ± 0.11
252	062	18:02:41.37–22:57:42.4	72 ± 9	24	0.51 ± 0.13
253	126	18:02:41.50–22:58:20.8	5 ± 2	2	0.33 ± 0.43
254	137	18:02:41.91–23:00:57.9	9 ± 3	3	-0.67 ± 0.28
255	061	18:02:42.19–22:57:52.1	30 ± 6	12	-0.87 ± 0.24
256	125	18:02:42.36–23:04:35.8	72 ± 9	13	-0.17 ± 0.11

Table 1—Continued

No	WID	CXOM20	Net Counts cts ks ⁻¹	SNR	Hardness Ratio
257	060	18:02:42.82–22:58:35.9	109 ± 11	40	-0.54 ± 0.11
258	100	18:02:42.95–23:03:12.4	123 ± 12	24	-0.59 ± 0.10
259	028	18:02:43.03–22:55:38.5	17 ± 4	6	0.24 ± 0.22
260	027	18:02:43.20–22:54:35.4	22 ± 5	7	-0.83 ± 0.27
261	099	18:02:43.51–23:01:35.4	58 ± 8	15	-0.06 ± 0.13
262	080	18:02:43.54–22:57:36.0	12 ± 4	5	-0.65 ± 0.29
263	124	18:02:44.04–22:57:15.6	5 ± 2	2	-0.50 ± 0.40
264	123	18:02:44.18–23:02:45.1	50 ± 8	11	-0.51 ± 0.14
265	145	18:02:44.76–22:58:15.4	8 ± 3	3	0.69 ± 0.34
266	079	18:02:44.78–22:59:51.9	47 ± 7	15	-0.37 ± 0.15
267	078	18:02:45.45–22:59:18.4	48 ± 7	14	-0.67 ± 0.17
268	136	18:02:45.46–22:58:37.4	9 ± 3	3	0.69 ± 0.34
269	144	18:02:45.74–22:59:44.2	9 ± 3	3	-0.38 ± 0.30
270	135	18:02:45.99–22:57:19.6	9 ± 3	3	0.86 ± 0.35
271	026	18:02:46.63–22:50:32.2	86 ± 11	13	-0.80 ± 0.12
272	051	18:02:46.95–22:53:22.5	10 ± 4	3	-0.09 ± 0.21
273	037	18:02:47.20–22:55:02.4	11 ± 4	4	-0.44 ± 0.26
274	044	18:02:47.49–22:48:20.4	42 ± 9	6	-0.20 ± 0.10
275	121	18:02:47.72–22:58:39.3	23 ± 5	8	-0.85 ± 0.25
276	120	18:02:47.82–22:59:42.2	22 ± 5	6	0.33 ± 0.22
277	036	18:02:47.90–22:49:11.5	57 ± 9	8	-0.61 ± 0.11
278	119	18:02:48.38–23:00:30.6	40 ± 7	12	-0.27 ± 0.14
279	077	18:02:48.63–22:59:32.4	73 ± 9	18	-0.82 ± 0.15
280	035	18:02:48.70–22:54:17.6	20 ± 5	6	-0.67 ± 0.25
281	043	18:02:48.75–22:51:57.1	13 ± 4	3	-0.58 ± 0.24
282	143	18:02:49.02–22:56:57.4	8 ± 3	3	-0.68 ± 0.28
283	076	18:02:49.16–22:59:45.5	120 ± 11	27	-0.32 ± 0.10
284	042	18:02:49.24–22:50:18.7	71 ± 10	11	-0.41 ± 0.11
285	025	18:02:49.36–22:48:32.6	93 ± 12	10	0.11 ± 0.07
286	041	18:02:49.66–22:48:55.6	100 ± 12	12	-0.59 ± 0.07
287	098	18:02:49.84–22:58:49.6	26 ± 5	9	-0.77 ± 0.25
288	142	18:02:50.12–23:00:13.4	12 ± 4	3	-0.75 ± 0.31

Table 1—Continued

No	WID	CXOM20	Net Counts cts ks ⁻¹	SNR	Hardness Ratio
289	056	18:02:50.36–22:47:41.0	37 ± 10	4	0.20 ± 0.09
290	034	18:02:50.52–22:48:50.3	93 ± 12	11	-0.55 ± 0.07
291	134	18:02:51.37–23:02:07.4	16 ± 4	4	0.71 ± 0.23
292	118	18:02:51.71–23:02:34.3	184 ± 15	26	-0.60 ± 0.08
293	050	18:02:52.27–22:49:48.8	18 ± 6	3	0.03 ± 0.13
294	150	18:02:53.09–23:03:39.0	22 ± 6	5	0.38 ± 0.15
295	149	18:02:54.90–22:58:22.1	14 ± 4	4	0.83 ± 0.27
296	023	18:02:57.08–22:54:20.1	168 ± 14	22	-0.67 ± 0.09
297	153	18:02:57.55–23:02:54.4	21 ± 6	4	-0.46 ± 0.18
298	148	18:02:57.83–23:00:46.4	13 ± 5	3	0.24 ± 0.22
299	141	18:02:58.06–22:56:02.4	13 ± 4	3	0.17 ± 0.21
300	033	18:03:00.19–22:52:55.7	89 ± 12	11	-0.47 ± 0.10
301	147	18:03:01.61–23:00:53.6	25 ± 6	5	-0.29 ± 0.16
302	152	18:03:02.19–23:02:48.7	45 ± 9	6	0.58 ± 0.13
303	146	18:03:03.32–23:00:19.2	25 ± 7	4	-0.19 ± 0.15
304	133	18:03:03.93–23:01:04.2	79 ± 11	10	-0.58 ± 0.11

Table 2. Summary of selected X-ray sources

No ^a	WID ^a	CXOM20	Net ^b	SNR ^b	max ^c cts ks ⁻¹	min ^c cts ks ⁻¹	ratio ^c	Prob. ^d const	hardness ^e ratio	2mass ^f	opti ^g	L _x (10 ³¹)
8	196	18:01:59.07-22:52:27.4	73	12	5.87±2.26	1.44±0.34	4.07±1.84	55%	-0.49±0.11	Y	[Y]	0.32
23	173	18:02:07.77-22:55:33.8	58	19	5.52±2.09	0.95±0.28	5.79±2.77	4%	-0.58±0.15	TTS	[Y]	0.27
38 (TC4)	347	18:02:12.47-23:05:48.0	62	9	2.34±1.92	1.06±0.35	2.21±1.96	100%	0.67±0.13	Y?	N	1.9
91 (C2)	235	18:02:23.05-23:01:58.1	857	129	15.99±3.05	9.72±0.52	1.65±0.33	2%	-0.47±0.03	N	N	6 ^h
94 (CD)	234	18:02:23.16-23:02:00.2	831	119	15.19±2.99	6.79±2.22	2.24±0.85	79%	-0.50±0.03	Y	[Y]	14 ^h
97	272	18:02:23.25-23:01:34.9	48	12	3.15±1.76	1.03±0.29	3.06±1.91	8%	-0.18±0.13	YSO	N	0.22
102 (A)	230	18:02:23.54-23:01:50.9	884	114	19.95±3.34	9.88±3.89	2.02±0.87	46%	-0.89±0.04	Y	[Y]	2
106 (B)	229	18:02:23.71-23:01:45.4	299	47	8.34±2.40	3.15±1.76	2.65±1.67	100%	-0.64±0.07	Y	Y	5
117 (TC1)	264	18:02:25.16-23:01:26.7	41	15	2.37±1.63	0.69±0.27	3.44±2.72	100%	0.24±0.16	N	N	4.7
166	212	18:02:30.37-22:59:29.0	135	57	8.78±2.43	2.26±0.32	3.88±1.21	0%	-0.19±0.09	YSO	U	0.62
170	211	18:02:30.93-23:02:35.6	73	21	4.29±1.95	1.27±0.30	3.37±1.73	68%	-0.79±0.15	N	Y	0.33
194	291	18:02:32.75-23:04:21.0	74	14	5.71±2.18	1.25±0.32	4.56±2.08	2%	-0.58±0.13	(YSO)	[Y]	0.34
211	72	18:02:34.51-22:59:37.9	312	107	9.98±2.55	2.77±1.69	3.60±2.38	43%	-0.47±0.06	Y	[Y]	1.1
237	29	18:02:38.85-22:50:06.0	81	13	5.57±2.20	1.79±0.35	3.12±1.38	2%	0.24±0.09	(YSO)	N	6.32
246	63	18:02:40.42-22:57:53.3	58	23	4.37±1.93	1.01±0.28	4.31±2.25	57%	-0.86±0.17	Y	[Y]	0.25
256	125	18:02:42.36-23:04:35.7	72	13	13.82±4.52	1.55±0.34	8.90±3.51	0%	-0.17±0.11	N	N	0.33
283	76	18:02:49.16-22:59:45.4	120	27	9.46±2.53	2.01±0.33	4.72±1.48	3%	-0.32±0.10	YSO	[Y]	0.55
285	25	18:02:49.36-22:48:32.5	93	10	10.05±2.80	2.71±0.44	3.70±1.19	2%	0.11±0.07	N	N	6.2

^aX-ray source numbers are from Table 1, and in the parenthesis, components A-D of HD164492 and TC1 and TC4 (massive protostellar cores from Cernicharo et al. (1998)) are marked. WID is source number identified by wavelet analysis.

^bThe net counts, and SNR is detection signal to noise obtained from wavelet analysis

^cThe count rate at the maximum count in the bin and at the minimum count in the bin (see the text for detail), and the ratio is the ratio between the two.

^dProbability of constancy which is estimated using χ^2 test.

^eHardness ratio: spectral hardness ratio = (H-S)/(H+S) where H and S is the count rate for hard (2-8 keV) and soft (0.5-2 keV) bands, respectively.

^fTTS and YSO are identified using JHK color diagram (details are described in Rho et al (2001)). Y: 2MASS detection, N: 2MASS non-detection. The identification with the parenthesis is uncertain classification due to uncertain 2MASS photometry.

^gOptical counterparts. Y: detection, the sources in the Guide star catalog are marked []. N: non-detection. U: uncertain.

^h14×10³¹ and 6×10³¹ erg s⁻¹ are soft and hard components, respectively, for CD-C2 blend spectrum.

Fig. 1 is a color figure which is available in jpeg format.

Fig. 1.— Three color *Chandra* ACIS-I image of the Trifid Nebula. The red, green and blue represents the images of 0.5-1 keV, 1-2 keV and 2-8 keV, respectively. The image is centered at R.A. $18^{\text{h}}02^{\text{m}}26^{\text{s}}$ and Dec. $-23^{\circ}00'39''$ (J2000) and covers 7.5 arcmin field of view.

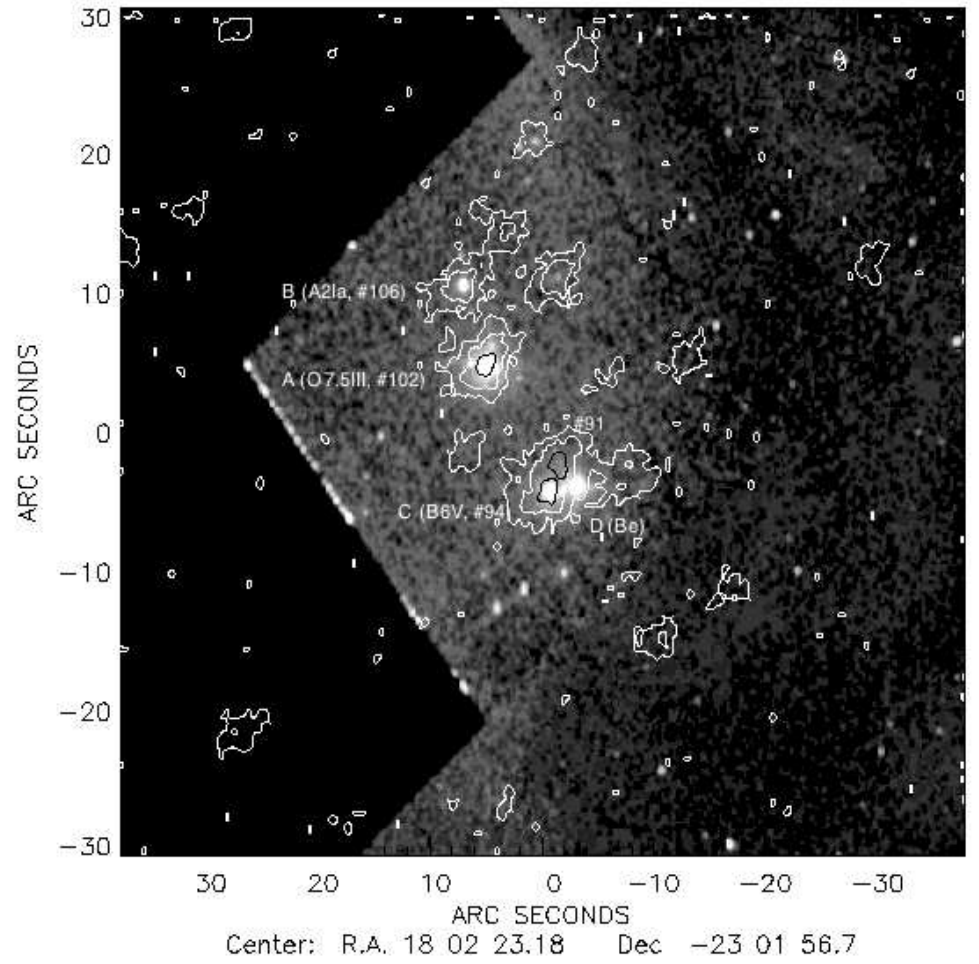


Fig. 2.— Sources in HD164492 complex. The gray scale image of HST superposed on *Chandra* X-ray contours. The components of HD164492 are marked.

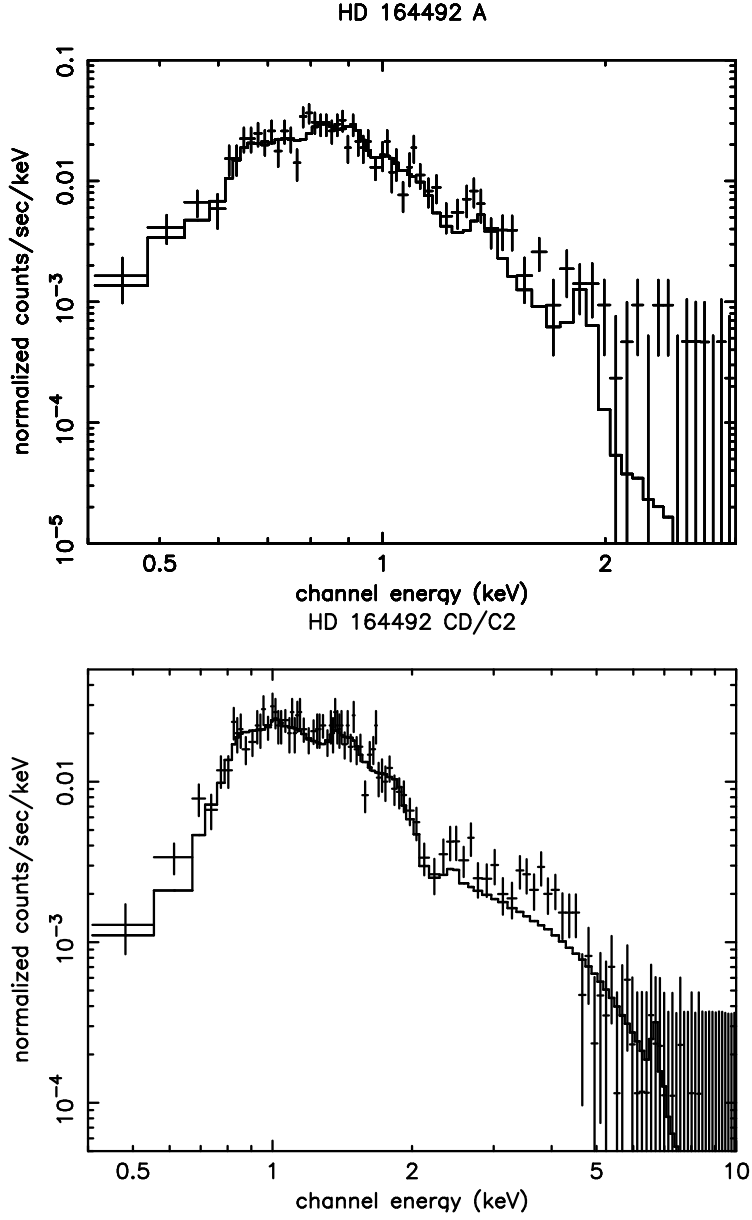


Fig. 3.— X-ray spectra of HD 164492 A, O7.5III star (a) and HD 164492 CD-blend, B/Be stars (b)

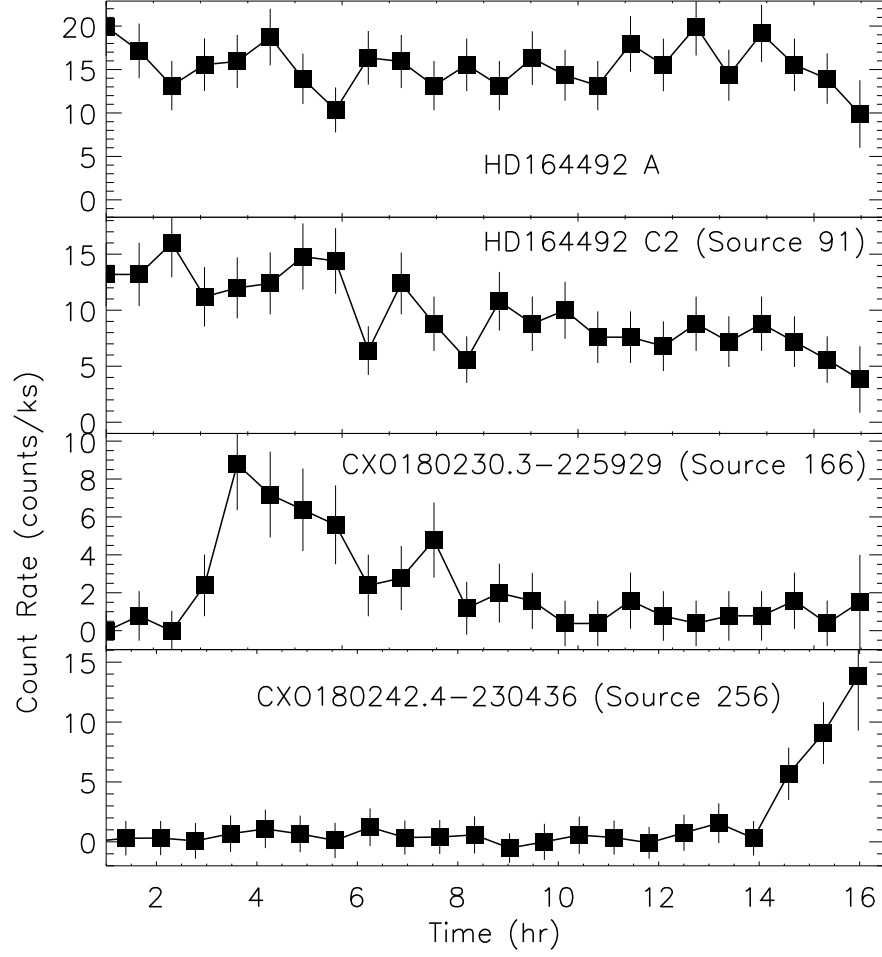


Fig. 4.— Light curves from HD164492 A and C2, and two pre-main-sequence stars. The source numbers are marked for each (see Table 1)

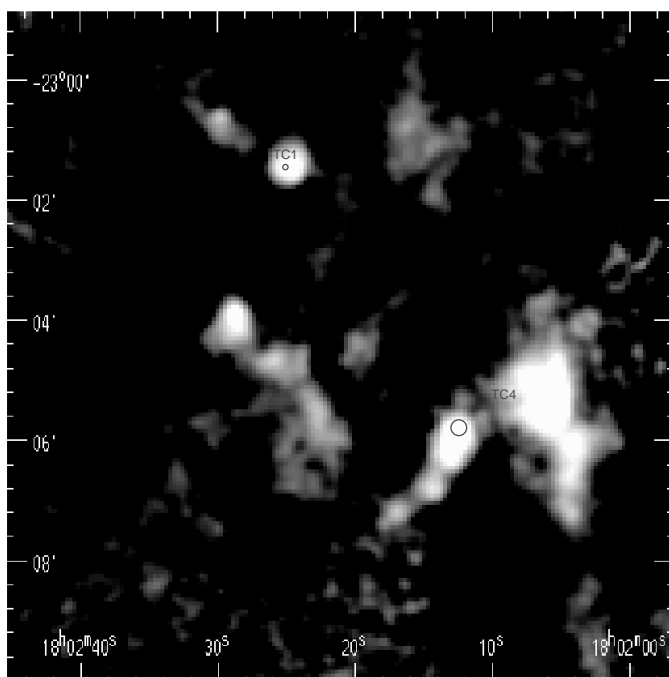


Fig. 5.— Thirteen hundred-micrometer dust continuum map (Cernicharo et al. 1998) and two X-ray sources coinciding with two of the earliest protostellar cores of TC1 and TC4.

This figure "f1color.jpg" is available in "jpg" format from:

<http://arxiv.org/ps/astro-ph/0401377v1>